Active learning prediction and experimental confirmation of atomic structure and thermophysical properties for liquid $Hf_{76}W_{24}$ refractory alloy

K. L. Liu, R. L. Xiao, Y. Ruan,* and B. Wei

MOE Key Laboratory of Materials Physics and Chemistry under Extraordinary Conditions, School of Physical Science and Technology, Northwestern Polytechnical University, Xi'an 710072, China

(Received 26 May 2023; accepted 18 October 2023; published 21 November 2023)

The determination of liquid atomic structure and thermophysical properties is essential for investigating the physical characteristics and phase transitions of refractory alloys. However, due to the stringent experimental requirements and underdeveloped interatomic potentials, acquiring such information through experimentation or simulation remains challenging. Here, an active learning method incorporating a deep neural network was established to generate the interatomic potential of the $Hf_{76}W_{24}$ refractory alloy. Then the achieved potential was applied to investigate the liquid atomic structure and thermophysical properties of this alloy over a wide temperature range. The simulation results revealed the distinctive bonding preferences among atoms, that is, Hf atoms exhibited a strong tendency for conspecific bonding, while W atoms preferred to form an interspecific bonding. The analysis of short-range order (SRO) in the liquid alloy revealed a significant proportion of icosahedral (ICO) and distorted ICO structures, which even exceeded 30% in the undercooled state. As temperature decreased, SRO structures demonstrated an increase in larger coordination number (CN) clusters and a decrease in smaller CNs. The alterations of the atomic structure indicated that the liquid alloy becomes more ordered, densely packed, and energetically favorable with decreasing temperature, consistent with the obtained fact: Both density and surface tension increase linearly. The simulated thermophysical properties were close to experimental values with minor deviations of 2.8% for density and 3.4% for surface tension. The consistency of the thermophysical properties further attested to the accuracy and reliability of active learning simulation.

DOI: 10.1103/PhysRevE.108.055310

I. INTRODUCTION

Investigating the atomic structure and thermophysical properties of liquid alloys has always been a top priority in studying liquid-liquid phase transition, amorphous formation, and solidification [1–3]. However, obtaining these properties for refractory alloys is challenging due to their extremely high melting points. Refractory alloys are highly valued in aerospace, military, and nuclear industry thanks to their exceptional radiation and corrosion resistance, mechanical properties, and thermostability [4,5]. Among them, the Hf-W binary alloy is a representative refractory alloy system, as Hf and W are the most commonly used refractory elements in many refractory alloys [6]. Additionally, it has been found that the Hf-W system has amorphous forming ability and large spin Hall effect [7,8]. The thermophysical properties referring to the density, specific heat, surface tension, and viscosity are the most basic physical characteristics of liquid alloys [9–12]. Understanding the atomic structure and thermophysical properties is beneficial to comprehend the physical characteristics and phase transitions of refractory alloys.

The measurement of the atomic structure and thermophysical properties of liquid refractory alloys, particularly in their undercooling state, was previously considered almost impossible until the invention of electrostatic levitation technology (ESL) [13,14]. Nevertheless, for some refractory alloys, the measurements are still not feasible due to the stringent experimental requirements. Even with ESL technology, the temperature range that can be obtained is not wide enough to cover all regions from superheated to undercooled states. In consequence, simulation has become a more efficient and universal way to approach these properties.

Conventional simulation methods include molecular dynamics (MD) and *ab initio* MD (AIMD), which are unsuitable for this task because MD relies on empirical potentials which have not been fully developed for refractory alloys, while AIMD is constrained to small time and space scales due to its expensive computational cost. To solve these problems, machine learning interatomic potential (MLIP) methods [15–18] have been developed. MLIP methods utilize the atom trajectories generated by AIMD as a dataset to develop interatomic potentials through machine learning. The potential integrates with MD, providing simulations with both accuracy and efficiency. The application of the deep neural network (DNN) in MLIP has yielded promising outcomes in accurately describing properties and performances of alloys, such as describing the martensitic transformations of NiTi shape memory alloy [19] and the mechanical property under the fusion service environment of pure W [20]. The DNN is also proved effective in the simulation of liquid alloys. The liquid structure of the Al-Cu-Ni system was accurately modeled [21]. Our group had developed a DNN potential to simulate the thermophysical properties and atomic structure of multicomponent Ti alloys

*Corresponding author: ruany@nwpu.edu.cn

 ©2023 American Physical Society

[22,23]. Compared with solid alloys, simulating liquid alloys requires higher computational demands, as it needs more AIMD calculations. To enhance efficiency without sacrificing accuracy, MLIP methods have incorporated active learning that exploit the correlation between data and model uncertainty to select the most informative samples for annotation [24].

In this paper, we proposed an active learning method based on the Deep Potential Generator (DPGEN) [25] to generate a DNN interatomic potential of $Hf_{76}W_{24}$ alloy efficiently. Combining with this, a deep potential MD (DPMD) was conducted to investigate the atomic structure and thermophysical properties of $Hf_{76}W_{24}$ refractory alloys. The accuracy and reliability of the method were verified by comparing with the simulated results from AIMD and experimental values using the ESL technique. Additionally, an analysis of structural features and short-range order (SRO) of the liquid alloy was conducted.

II. METHODS

A. Materials and experiments

The $Hf_{76}W_{24}$ eutectic refractory alloy was prepared by melting pure Hf (99.99%) and pure W (99.99%) in an arc-melting furnace, which was filled with Ar after being pumped down to a pressure of 1.0×10^{-4} Pa. The samples were ∼2.4 mm in diameter and weighted ∼100 mg. The samples were levitated between two vertical electrodes coupled with four side electrodes in a chamber that was evacuated to 1.0×10^{-5} Pa. A continuous-wave SPI SP300 fiber laser with a wavelength of 1070 nm was employed to heat the sample, and the temperature was recorded using a Sensortherm GmbH M322 2-color pyrometer. Images of the sample were captured using a complementary metal-oxide semiconductor camera under ultraviolet background light with a frequency of 90–120 Hz. The volume V of the sample was determined using these images [26]. Then combined with the sample mass m, the density ρ of the liquid alloy was calculated by $\rho = m/V$.

For surface tension measurement, the levitated and molten sample was maintained at a specific temperature by adjusting the laser power. An AC voltage of 600 mV was then superimposed on the high-voltage amplitude to induce oscillation of the sample in an axisymmetric mode. Then the excitation was turned off, the resulting transient-free decay curve was detected by a THORLABS PDA100A2 amplified photoelectric detector. The characteristic frequency was analyzed from the decay curve using fast Fourier transform, and the surface tension was then derived from the equation [27]:

$$\omega_2^2 = \frac{2\sigma}{\pi^2 \rho r_0^3}, \tag{1}$$

where ω_2 was the characteristic frequency for the second-order oscillation, σ was the surface tension, ρ was the density we measured before, and r_0 was the semidiameter of the sample.

B. Simulation details

The simulation process for the liquid alloy consisted of three primary stages: preparation of the training dataset, generation of the DNN potential, and acquisition of the thermophysical properties and liquid structure.

To prepare the training dataset, VASP was employed for AIMD simulations. A supercell consisting of 200 atoms was created and heated up to 3000 K, well above the melting point. It was then relaxed for 10000 steps to achieve an equilibrium liquid alloy under periodic boundary conditions with a canonical ensemble (NVT) and a Nosé-Hoover thermostat. The volume of the supercell was adjusted to maintain an external pressure of ∼0 kbar. Subsequently, the supercell was cooled down and relaxed for 5000 steps at various temperatures: 2800, 2600, 2400, 2200, 1900, and 1500 K, generating the training dataset. The Perdew-Burke-Ernzerhof gradient approximation and projector augmented-wave pseudopotentials were used for the exchange-correlation functional, and only the Γ point was sampled for the Brillouin zone with an energy cutoff of 300 eV, a convergence threshold of 1×10^{-5} eV for electronic iteration, and a time step of 3 fs.

DPGEN automatically and iteratively performed three steps: exploration, labeling, and training. In the exploration step, LAMMPS [28] was employed. The initial conformations were selected from the training database randomly. The system was set as an isothermal-isobaric (NPT) ensemble with zero pressure, running for 10 000 steps with a sampling interval as 20. In the labeling step, VASP was employed to carry out the density functional theory calculations. Monkhorst-Pack grids were used, where the k-point mesh was set with a separation of 0.5 $Å^{-1}$.

In the training step, the DeePMD-kit [29] was utilized for the training of the DNN potential. In the DeePMD-kit, the energy of the system can be expressed as a sum of energy of each atom i: $E = \sum_i E_i$. The value of E_i is fully determined by the environment surrounding the ith atom, as most interactions can be captured within a sufficiently large cutoff radius [30]:

$$E_i = E_{s(i)}[\mathbf{R}_i, \{\mathbf{R}_j | j \in N_{R_c}(i)\}], \tag{2}$$

where N_{Rc} (i) denotes the index set of the neighbors of atom i within the cutoff radius R_c. Therefore, the atomic energy E_i can be obtained by training a neural network, where the inputs are the positions of atom i and its neighboring atoms. Considering the translational, rotational, and permutational symmetries in the system, a coordinate transformation of the atoms is needed before training, so a descriptor $\mathbf{D}_i$ is introduced:

$$\mathbf{D}_i = \mathbf{D}_i[\mathbf{R}_i, \{\mathbf{R}_j | j \in N_{R_c}(i)\}], \tag{3}$$

in a full radical and angular information considered system, D_{ij}^{α} can be expressed as

$$D_{ij}^{\alpha} = \left\{ \frac{1}{R_{ij}}, \frac{x_{ij}}{R_{ij}}, \frac{y_{ij}}{R_{ij}}, \frac{z_{ij}}{R_{ij}} \right\}, \tag{4}$$

where R_{ij} is the distance between i and j, and x_{ij}, y_{ij}, and z_{ij} are the local coordinates. After these preparations, a DNN $\mathcal{N}$ is introduced to map the descriptors to atomic energy:

$$E_i = \mathcal{N}_{(i)}(D_{ij}^{\alpha}). \tag{5}$$

The force and virial are given by:

$$\mathbf{F}_i = -\sum_{j\in N(i),\alpha}\frac{\partial \mathcal{N}_{(i)}}{\partial D_{ij}^{\alpha}}\frac{\partial D_{ij}^{\alpha}}{\partial \mathbf{R}_i} - \sum_{j\neq i}\sum_{k\in N(j),\alpha}\delta_{i,a(j)}\frac{\partial \mathcal{N}_{(j)}}{\partial D_{jk}^{\alpha}}\frac{\partial D_{jk}^{\alpha}}{\partial \mathbf{R}_i} - \sum_{j\neq i}\sum_{k\in N(j),\alpha}\delta_{i,b(j)}\frac{\partial \mathcal{N}_{(j)}}{\partial D_{jk}^{\alpha}}\frac{\partial D_{jk}^{\alpha}}{\partial \mathbf{R}_i} - \sum_{j\neq i}\sum_{k\in \bar{N}(j),\alpha}\delta_{i,k}\frac{\partial \mathcal{N}_{(j)}}{\partial D_{jk}^{\alpha}}\frac{\partial D_{jk}^{\alpha}}{\partial \mathbf{R}_i}, \tag{6}$$

$$\Xi = -\sum_{i\neq j}\mathbf{R}_{ij}\sum_{\alpha}\frac{\partial \mathcal{N}_{(i)}}{\partial D_{ij}^{\alpha}}\frac{\partial D_{ij}^{\alpha}}{\partial \mathbf{R}_{ij}} - \sum_{i\neq j}\delta_{j,a(i)}\mathbf{R}_{ij}\sum_{q,\alpha}\frac{\partial \mathcal{N}_{(i)}}{\partial D_{iq}^{\alpha}}\frac{\partial D_{iq}^{\alpha}}{\partial \mathbf{R}_{ij}}. \tag{7}$$

The parameters $\{\mathbf{W}_s^p, \mathbf{b}_s^p\}$ of the DNN are determined by a training process that minimizes the loss function L, which can be expressed as

$$L = \frac{p_\epsilon}{N}\Delta E^2 + \frac{p_f}{3N}\sum_i |\Delta \mathbf{F}_i|^2 + \frac{p_\xi}{9N}\|\Delta \Xi\|^2, \tag{8}$$

where ΔE, $\Delta \mathbf{F}_i$, and $\Delta \Xi$ are root mean square errors (RMSEs) and p_ϵ, p_f, and p_ξ are prefactors of energy, force, and virial, respectively. The cutoff radius was set to 6 Å, and the smooth cutoff radius was set as 5.8 Å to eliminate the discontinuity caused by the cutoff radius [21,22,30]. The embedding and fitting nets consisted of (25, 50, 100) and (240, 240, 240), respectively. An exponentially decaying learning rate from 1.00×10^{-3} to 3.51×10^{-8} was applied. The DPGEN ran nine iterations. The initial training dataset consisted of 10000 frames. During each iteration, 1000 frames were labeled and incorporated into the training set for next iteration. In each exploration step, a gradually decreasing temperature was set, until the 95% of the picked-out frames in last exploration step were all considered accurate.

Once the DNN potential was generated, LAMMPS was employed to perform the DPMD simulations. The simulation consists of 10 976 atoms within a simulation box with maximum dimensions of $63.3\times63.3\times63.3$ Å^3. The system was initially relaxed at 3000 K for 2×10^5 steps using an NPT ensemble for with a time step of 1 fs. The pressure was set to 0. The temperature was then decreased from 3000 to 1500 K at a cooling rate of 10^{12}K s^{-1}. At each temperature interval of 100 K, the system was equilibrated for 2×10^5 steps. Finally, another 1×10^5 steps were performed to collect the quantities. The density was then calculated using the simulation results and the appropriate equation:

$$\rho = (n_{\mathrm{Hf}}m_{\mathrm{Hf}} + n_{\mathrm{W}}m_{\mathrm{W}})/V, \tag{9}$$

where n_{Hf} and n_{W} are the numbers of Hf and W atoms, m_{Hf} and m_{W} are their absolute atomic masses, and V is the volume of the simulation system. The surface tension was calculated by the following equation [31,32]:

$$\sigma = \frac{V}{2A}\left\langle P_{xx} - \frac{1}{2}(P_{yy}+P_{zz})\right\rangle, \tag{10}$$

where V is the volume, A is the area of liquid-vapor interface, and P_{xx}, P_{yy}, and P_{zz} are the tangential components of the pressure tensor.

III. RESULTS AND DISCUSSION

A. Thermophysical properties of liquid alloy

The comparison of the energy and force on x between the DP and AIMD for the training and validation data is illustrated in Fig. 1. The validation data are not included in the training dataset. The energy and force generated by DP are very close to AIMD, thereby validating the accuracy of the training. The RMSE values for energy in training and validation are 2.15×10^{-3} and 3.67×10^{-3}eV atom^{-1}, respectively. As for force, corresponding RMSE values are 2.25×10^{-1} and 2.47×10^{-1} eV Å^{-1}.

The density and surface tension of the $Hf_{76}W_{24}$ eutectic refractory alloy were both measured and simulated, and the results are presented in Fig. 2. The red solid circles represent the experimental measurements, and the open squares and triangles represent the results obtained by DPMD simulations. The liquidus temperature of the alloy is $T_{\mathrm{L}} = 2283$ K. The experimental and simulated results are in satisfactory agreement, with only a small division of 2.8% in density and 3.4% in surface tension observed at the melting point. This consistency demonstrated that the calculated DNN potential is proficient in accurately predicting the macroscopic thermophysical properties of the alloy system. However, due to volatilization in overheating states, the experimental temperature range achieved is relatively narrow, from 2203 to 2449 K for the density measurement and from 2253 to 2373 K for the surface tension measurement, with a maximum undercooling of only 131 K ($0.06T_{\mathrm{L}}$). Fortunately, the simulations did not suffer from such issues, with a pretty wide temperature range from 1500 to 3000 K. Within this range, the differences between the experiment and simulation were no more than 3% for density and 3.4% for surface tension. The density of the liquid alloy was fitted as followed:

$$\rho_{\mathrm{ESL}} = 13.58 - 7.01\times10^{-4}(T - T_{\mathrm{L}}), \tag{11}$$

$$\rho_{\mathrm{DPMD}} = 13.20 - 4.54\times10^{-4}(T - T_{\mathrm{L}}). \tag{12}$$

The surface tension of the liquid alloy was expressed as

$$\sigma_{\mathrm{ESL}} = 1.46 - 2.15\times10^{-4}(T - T_{\mathrm{L}}), \tag{13}$$

$$\sigma_{\mathrm{DPMD}} = 1.41 - 1.39\times10^{-4}(T - T_{\mathrm{L}}). \tag{14}$$

Both the density and surface tension demonstrated a linear increase as temperature decreased, as observed in both experimental and simulated results. Such behavior has been extensively reported for various pure metals and alloys [33,34], including W and Hf [13,14]. It can be attributed to the reduction in thermal motion at lower temperatures, which enhances atomic interactions while reducing the average interatomic distance, resulting in increased density. Consequently, the enhanced atomic interaction increases the energy requirement for an atom moving to the surface from the interior, thus elevating the surface tension. DPMD enables simulations of larger scales and longer time scales while maintaining comparable accuracy with AIMD.

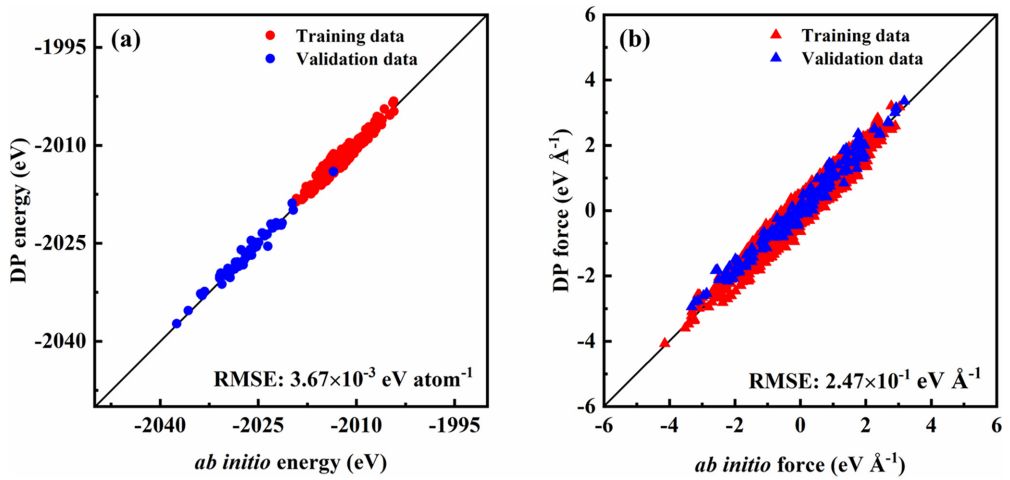

FIG. 1. Correlation between *ab initio* molecular dynamics (AIMD) and deep potential (DP) data: (a) energy and (b) force.

By employing a larger system size, the finite-scale effect [35] could be avoided, and the influence of thermal fluctuations on simulation results could be mitigated. Additionally, a longer simulation time ensures a thermodynamic equilibrium state of the system, enhancing the accuracy of prediction. The interatomic potential we developed provides a satisfactory description of the $Hf_{76}W_{24}$ alloy; however, its applicability to other compositions within the alloy system remains limited at present. In our forthcoming work, we plan to enhance the interatomic potential by incorporating training data from diverse compositions and nonequilibrium states, thereby achieving comprehensive transferability across the entire alloy system.

B. Statistical features of the liquid alloy

Liquid alloys are typically characterized by a combination of SRO and long-range disorder, and in some cases middle-range order (MRO) has also been observed [36,37].

Pair distribution functions (PDFs) give the joint probability of finding two particles at particular positions in the system, defined as [38]

$$g_{ij}(r) = \frac{V}{N_i N_j} \sum_{i=1}^{N} \frac{n_{ij}(r, \Delta r)}{4\pi r^2 \Delta r}, \tag{15}$$

where i, j represents the type of the central atom and its neighboring atom, and n_{ij} $(r, \Delta r)$ is the number of atoms j in the sphere shell centered on atom i from r to $r + \Delta r$. At each simulated temperature, Figs. 3(a)–3(d) compare the total and partial PDFs obtained from both AIMD and DPMD. The open circle representing AIMD in the figures closely aligns with the solid line representing DPMD, proving the accuracy of the simulation of the liquid structure. At 1900 K, the W-W atomic pair exhibits the closest proximity of the first peak at 2.6 Å and the highest peak at 3.1 Å among all atomic pairs, indicating that the distance between W-W atoms is shorter than other pairs due to a smaller atomic radius of W (130 pm) compared with Hf (144 pm). The simulation exhibits a considerable resemblance to the experimental observed atomic structure of Hf-W amorphous thin films prepared by ion-plasma sputtering [8]. Despite the difference in states, this comparison

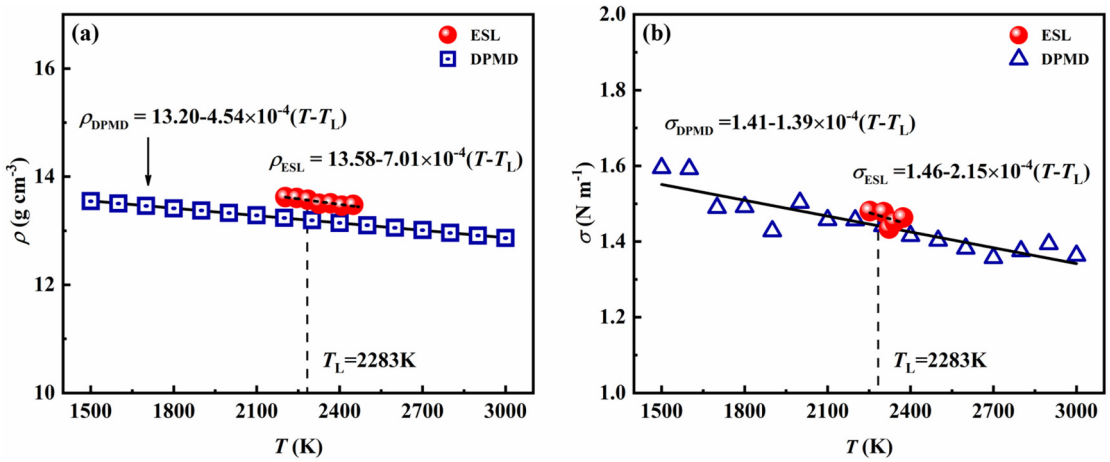

FIG. 2. Thermophysical properties of liquid $Hf_{76}W_{24}$ alloy at different temperature: (a) density and (b) surface tension.

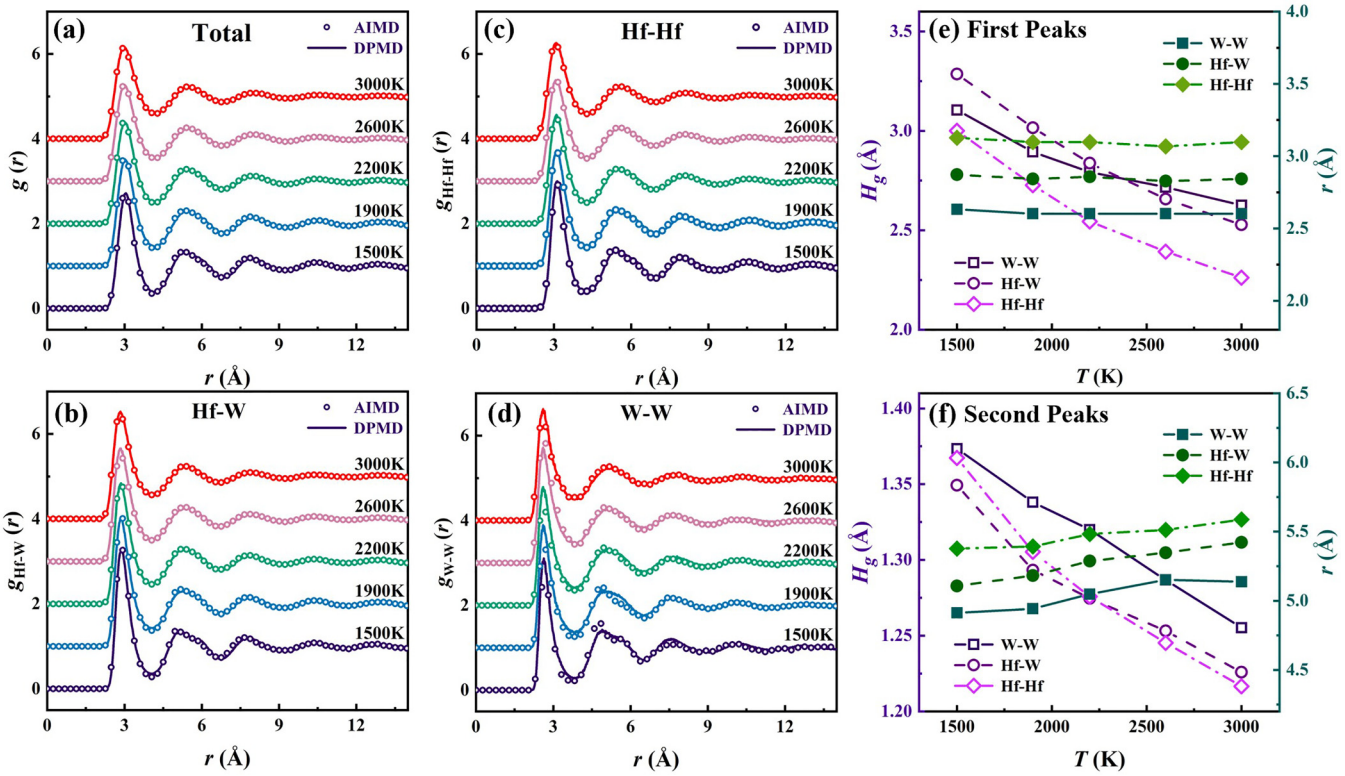

FIG. 3. Pair distribution functions (PDFs) of liquid $Hf_{76}W_{24}$ alloy at different temperatures: (a) total PDFs, (b)–(d) partial PDFs, and (e)–(f) height and location of first and second peaks in partial PDFs.

can still provide us with valuable information owing to the correlation between the atomic structure of amorphous and its liquid state [39]. Specifically, the positions of the first and second peaks as well as the splitting of the second peak in the PDFs show significant correspondence, indicating the presence of short- and middle-range clusters in the liquid atomic structure. Figures 3(e) and 3(f) present more detailed statistics of PDFs, illustrating the changes in peak height and peak position at different temperatures. The position of the first peak remains relatively stable as the temperature decreases, while the peak height increases significantly. Furthermore, the shift in the center position of the second peak also provides direct evidence of its splitting tendency in Fig. 3(f). This tendency corresponds to the MRO clusters formed by the combination of SRO clusters, indicating the increased stability of the liquid structure, which is conducive to the formation of amorphous phase [39,40].

To determine the chemical short-range order (CSRO) in the liquid alloy, partial coordination numbers (CNs) and Warren-Cowley parameters were calculated based on the partial PDF, as shown in Fig. 4. The partial CN Z_{ij} represents the number of j atoms in the first nearest-neighbor distance of the central atom i, defined as [38,41]

$$Z_{ij} = \int_0^{r_{\min}} 4\pi r^2 \rho_j g_{ij}(r) dr, \tag{16}$$

where $r_{\min}$ represents the position of first valley in partial PDF $g_{ij}(r)$, and ρ_j is the average number density of j atom. As demonstrated in Fig. 4(a), N_{Hf-Hf} and N_{W-Hf} increase as the temperature decreases, while the changes in N_{W-W} and N_{Hf-W} are less noticeable and N_{W-W} slightly decreases. Since the W content in the liquid alloy components is much less than that of Hf, N_{W-W} and N_{Hf-W} are significantly smaller than N_{Hf-Hf} and N_{W-Hf}. The Warren-Cowley parameter α_{ij} is utilized to characterize the deviation of local chemical components from a completely random solution within the nearest-neighbor range. It is defined as [42]

$$\alpha_{ij} = 1 - Z_{ij}/c_j Z_j, \tag{17}$$

where Z_{ij} is the partial CN, c_j is the chemical component of atom j, and Z_i is the CN of the i atom which equals $Z_{ii} + Z_{ij}$. In a completely disordered system, $\alpha_{ij} = 0$. If $\alpha_{ij} < 0$, it means that this type of pair is more likely to form, while if $\alpha_{ij} > 0$, the probability of this type of pair forming is small. Figure 4(b) illustrates that Hf atoms have a greater tendency to bond with Hf atoms, while W atoms exhibit a lower inclination to do so. The dash-dotted line serves as a reference, indicating $\alpha_{ij} = 0$ in a completely disordered liquid. As observed, $\alpha_{Hf-Hf} \sim 0$, indicating that this tendency is not very prominent. In the system, W-W has the smallest CN, and $\alpha_{W-W} \gg 0$, while W-Hf has a relatively large CN, and α_{W-Hf} is negative, indicating that W atoms are more inclined to bond with different kinds of atoms. For Hf atoms, bonding between the same types of atoms is more preferred.

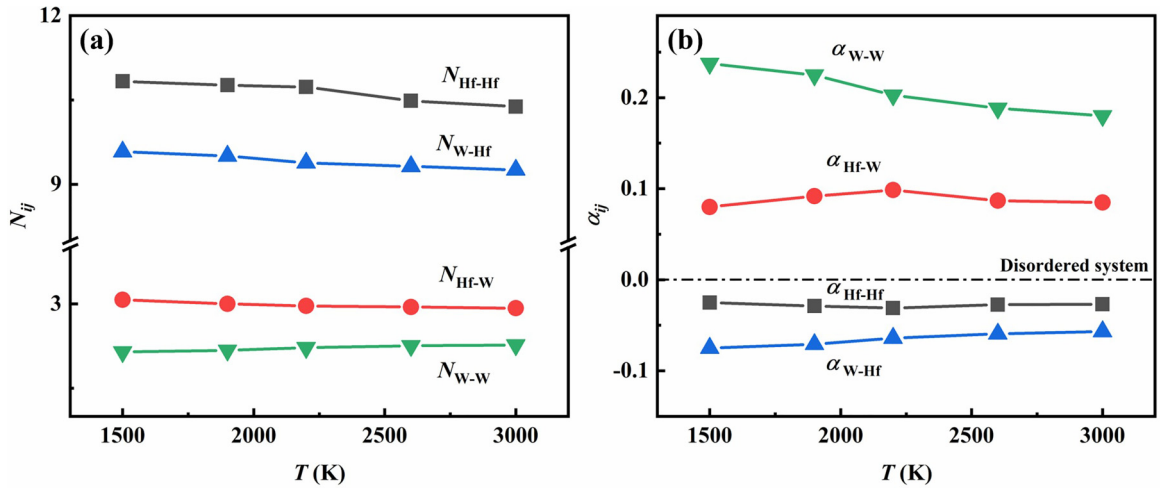

FIG. 4. Bonding features of liquid $Hf_{76}W_{24}$ alloy at different temperature: (a) partial coordination number and (b) Warren-Cowley parameter.

The bond-angle distribution (BAD) function, which characterizes the distribution of angles between two bonds in ternary atoms, is commonly utilized to describe liquid structure and suggest the type of SRO. The bond angel θ_{ijk} between ijk atoms is defined as [38]

$$\theta_{ijk} = \cos^{-1}\left(\frac{r_{ij}^2 + r_{ik}^2 + r_{jk}^2}{2r_{ij}r_{ik}}\right), \tag{18}$$

where r_{ij}, r_{ik}, and r_{jk} are the bond length between the nearest atoms ij, ik, and jk, respectively. The BADs are calculated by the following equation [38]:

$$P(\theta) = \frac{1}{\sum_{i=1}^{N} N_i(N_i-1)} \sum_{i=1}^{N}\sum_{j=1}^{N_i}\sum_{k=j+1}^{N_i} \delta(\theta - \theta_{ijk}). \tag{19}$$

After normalization, the BADs obtained by both AIMD and DPMD were compared, as shown in Fig. 5. The curves obtained from DPMD and AIMD simulations exhibit a high degree of similarity, implying that DPMD is an effective method for describing the liquid structure of the Hf-W system. The BADs display two main peaks. The locations of the two primary peaks are marked by the dash-dotted line in Fig. 5. As temperature decreases, the peaks of BADs become sharper, indicating the formation of more ordered structure at lower temperature. The positions of the two peaks suggest the types of SRO that exist in the liquid alloy [43–45]. The first peak of the total BAD is situated at 58°, while the second peak is located at 108°. As for Hf-W-Hf, the peaks are at 61° and 115°, respectively, whereas for Hf-W-W, they are at 57° and 112°. These distributions are close to the icosahedral (ICO) structure with peaks at 63.4° and 116.4°, indicating that the liquid alloy contains the ICO and distorted ICO (dis-ICO) structures. The BADs of Hf-Hf-W and W-Hf-W ∼53° and 100°, respectively, suggest the presence of a body-centered cubic (BCC) structure. The BADs of Hf-Hf-Hf and W-W-W are attributed to the composite formation of face-centered cubic, hexagonal close-packed, and ICO structures. The peak located ∼150° indicates that a tetrahedron and some other complex polyhedrons are likely to form and further contribute to the degree of local order increasing.

C. SRO in the liquid alloy

The Honeycutt-Anderson (HA) common neighbor analysis was introduced to provide a more detailed characterization of the common neighbors of an atom pair and to offer a clear atomic configuration of SRO. The HA analysis employs four indices (i, j, k, l) to describe the bonding structure of the neighboring and central atoms [46]. For a central atom α and one of its neighboring atoms β, i indicates the presence or absence of a bond between α and β, j represents the number of bonds shared by both α and β, k denotes the number of bonds among these j atoms, while l is used to differentiate cases where these exponents are still indistinguishable. Figure 6 displays the atomic conformations selected from the liquid alloys, with red atoms representing central atom α, blue atoms representing neighboring atom β, and green atoms representing those bonded to both β and α. The figure also shows how the HA indices change as temperature decreases. The results indicate that the most abundant type of structure in the liquid alloy is the ICO structure, represented by the HA index 1551, followed by the dis-ICO structure (HA indices 1541 + 1431) and then the BCC structure (HA indices 1661 + 1441). The remaining types of structures are less abundant. As temperature decreases, the number of regular ICO structures in the liquid alloy increases sharply from 18 to 38%, while the number of BCC structures increases from 8 to 11%. Conversely, the number of dis-ICO structures decreases from 19 to 15% due to the conversion of some dis-ICO structures into ICO structures.

In the analysis of SRO in liquid structures, both simulation time and system scale could have influences on the results, particularly in deep undercooling states where sufficient equilibration time is required [47]. The statistical accuracy of liquid structure factors can be enhanced with a large number of atoms in the system. With DPMD, we can obtain more sufficient simulation conditions, allowing for a system scale

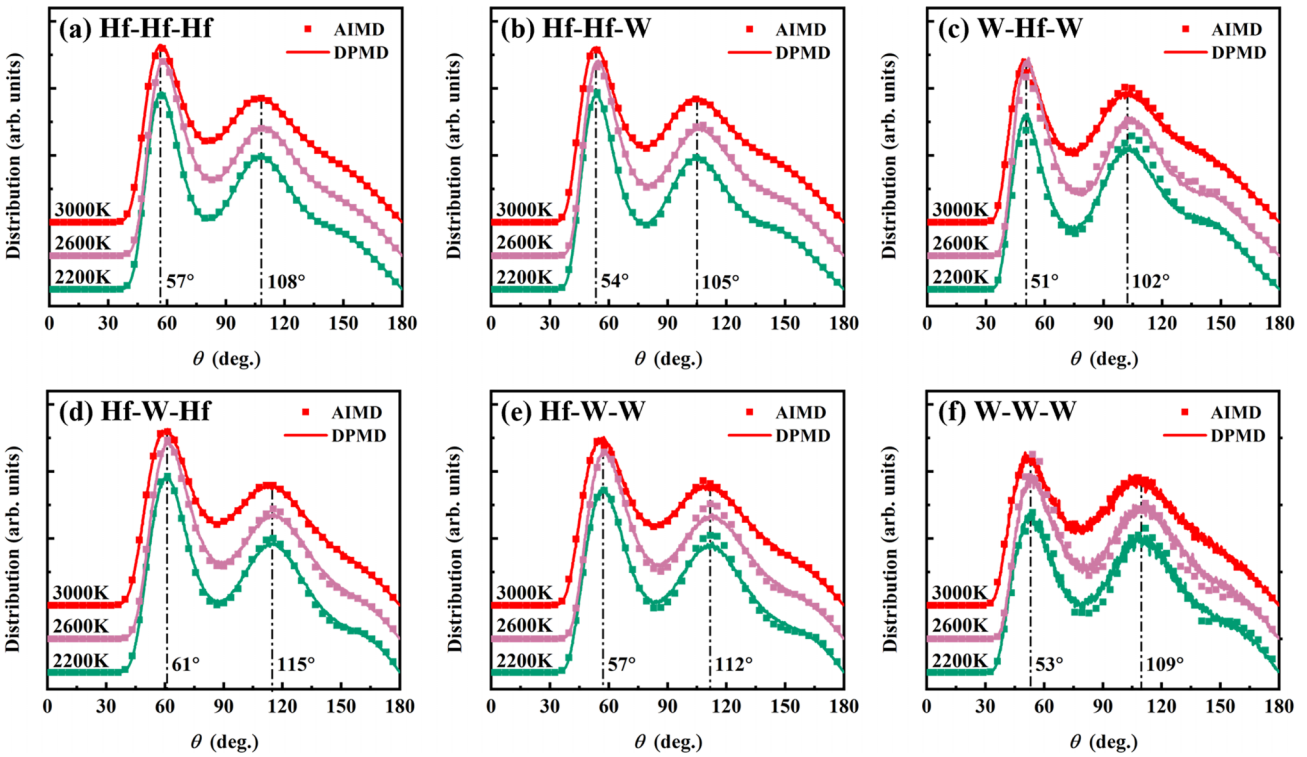

FIG. 5. Partial bond-angle distributions of liquid $Hf_{76}W_{24}$ alloy at different temperatures: (a) Hf-Hf-Hf, (b) Hf-Hf-W, (c) W-Hf-W, (d) Hf-W-Hf, (e) Hf-W-W, and (f) W-W-W.

up to 10^4 atoms, and the simulation time up to 10^2 ps, fulfilling the requirements for simulations.

To further investigate the SRO in the liquid alloy [48],Voronoi polyhedral (VP) analysis was employed to reveal the atomic arrangement of them. VP is a convex polyhedron defined by the perpendicular bisectors of the bonds between the central atom and its nearest neighbors. VP is described by a set of indices $\langle n_3, n_4, n_5, n_6, \cdots \rangle$, where n_i denotes the number of faces with i sides. The sum of n_i is the CN of the central atom. Figures 7(a) and 7(b) present the top 10 VPs with the highest content in liquid alloys for Hf and W centered atoms, and Figs. 7(c)–7(e) display the CNs of each type of central atom. The atomic conformations corresponding to their VP indices are also presented in Fig. 7, where the red atoms represent Hf and the blue atoms represent W. The VP indices found in liquid alloys can be roughly classified into two categories: ICO-like and others. ICO-like include ICO and dis-ICO indices such as $\langle 0\,0\,12\,0 \rangle$ and $\langle 0\,1\,10\,2 \rangle$, while others include indices such as $\langle 0\,3\,8\,2 \rangle$ and $\langle 0\,4\,6\,3 \rangle$. As the temperature decreases, the content of ICO-like VPs increases rapidly, surpassing the growth rate of the other types. Simultaneously, the trend of total CNs indicates an increase in the proportion of VPs with higher CNs (CN = 13, 14, 15), while a decrease is observed for those with lower CNs (CN = 10, 11, 12). This trend indicates an increase in the orderliness and compactness of the liquid

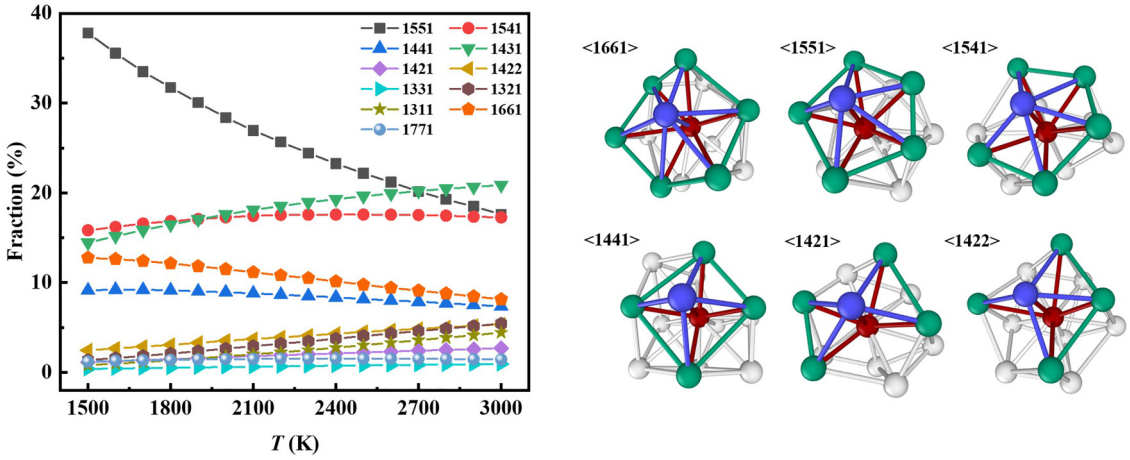

FIG. 6. Honeycutt-Anderson (HA) analysis of liquid $Hf_{76}W_{24}$ alloy and atomic conformations of typical indices.

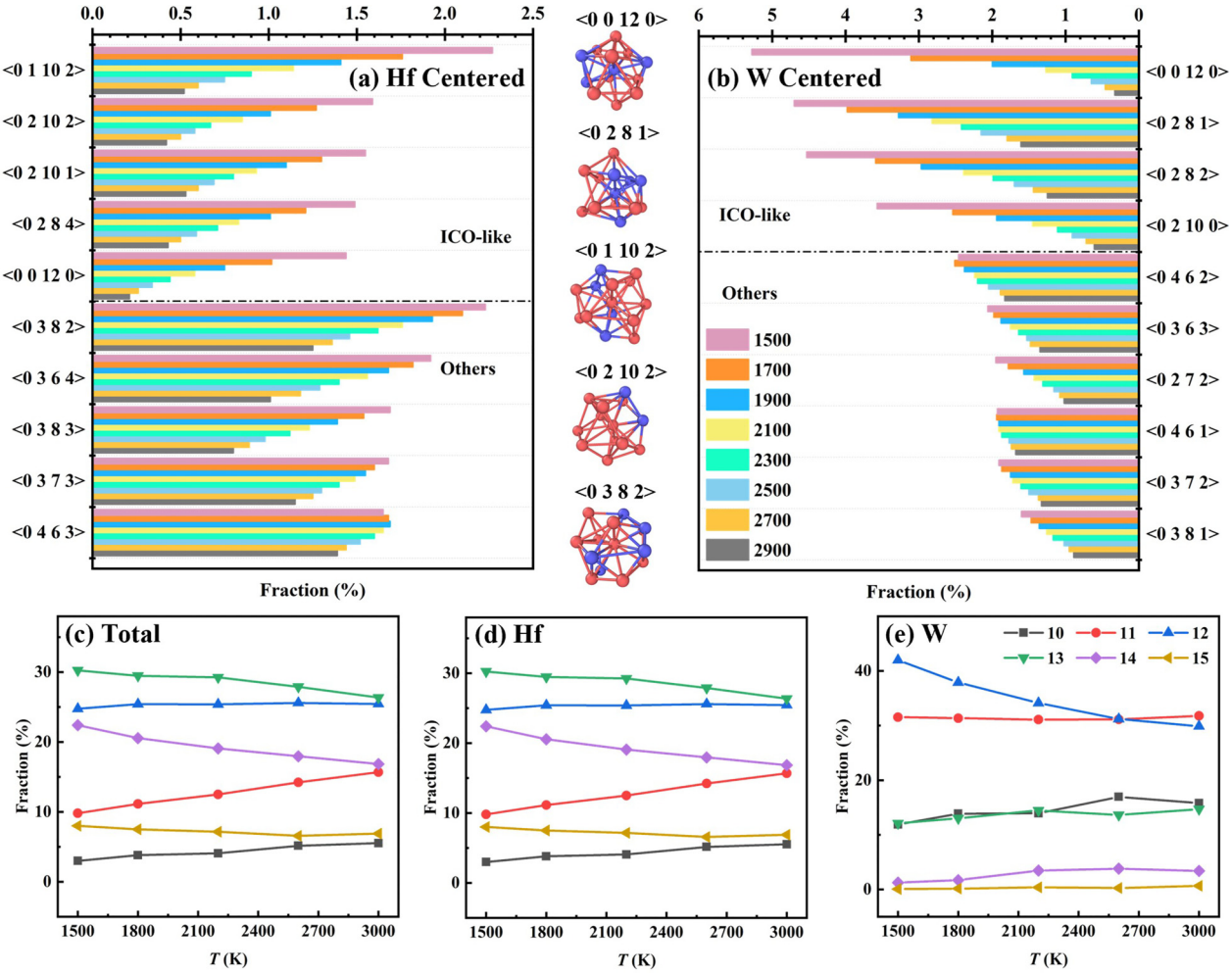

FIG. 7. Voronoi polyhedral (VP) analysis of liquid $Hf_{76}W_{24}$ alloy at different temperature: (a) and (b) Hf and W centered VP indices and (c)–(e) total and partial coordination numbers.

alloy, confirming the observed changes in thermal physical properties with temperature [49]. Additionally, there are notable distinctions between VPs centered on W and Hf. VPs centered on W have the highest content at a CN of 12, which can exceed 30%, suggesting that they contain more ICO-like type. The W-centered VP indices also confirm that ICO-like clusters represented by $\langle 0\,0\,12\,0\rangle$ account for the largest percentage, and the change with temperature is substantial. The Hf-centered VPs have higher CNs, with an average of 12.91 at 1500 K, while that with W-centered VPs is 11.63. Within the Hf-centered VPs, CN = 15 accounted for at least 8%, CN = 14 accounted for at least 17%. The variation of the content of VPs with decreasing temperature is consistent with the change of the total CN: The content of high coordination clusters increases, while the content of low coordination clusters decreases.

IV. CONCLUSIONS

In summary, we constructed the interatomic potential of the $Hf_{76}W_{24}$ refractory alloy applying an active learning method incorporating a DNN. The potential was applied in DPMD to investigate the atomic structure and thermophysical properties of the liquid alloy over a wide temperature range. The comparison of the simulated atomic structure with AIMD results verified the accuracy of the DNN potential, as both exhibited consistent characteristics. The simulation showed that the peak of the PDFs increased with the decreasing temperature, indicating the enhancement of the orderliness of the liquid alloy. The CNs and CSRO values demonstrated that the local environment surrounding W and Hf atoms was distinct, with W atoms tending to bond with Hf atoms, and Hf atoms preferring to bond with other Hf atoms. The BADs suggested the existence of SRO clusters in the liquid alloy. The type and atomic configurations of the clusters were analyzed using HA and VP, confirming the presence of a substantial number of ICO-like clusters in the liquid alloy. The content of the ICO-like clusters increased substantially with decreasing temperature. The CN of clusters centered on W is different from that centered on Hf, the former has more clusters with CN = 12 and the latter featuring a higher proportion of clusters with CN values of 14 and 15.

The density and surface tension of the alloy were measured using ESL technology. The simulated thermophysical properties were close to the experimental values with the difference of 2.8% in density and 3.4% in surface tension. Both increased

linearly as the temperature decreased. The change of liquid atomic structure indicated that the liquid alloy became more ordered, densely packed, and had lower energy when the temperature decreased, which confirmed the change of thermophysical properties. The consistency of the thermophysical properties further proved the accuracy and reliability of active learning simulation.

ACKNOWLEDGMENTS

Financial supports from the National Natural Science Foundation of China (Grants No. 52225406, No. 52073232, and No. 52088101) and the Science Fund for Scientific and Technological Innovation Team of Shaanxi Province (Grant No. 2021TD-14).

[1] M. Guerdane, H. Teichler, and B. Nestler, Local atomic order in the melt and solid-liquid interface effect on the growth kinetics in a metallic alloy model, Phys. Rev. Lett. **110**, 086105 (2013).

[2] W. Xu, M. T. Sandor, Y. Yu, H. B. Ke, H. P. Zhang, M. Z. Li, W. H. Wang, L. Liu, and Y. Wu, Evidence of liquid-liquid transition in glass-forming $La_{50}Al_{35}Ni_{15}$ melt above liquidus temperature, Nat. Commun. **6**, 7696 (2015).

[3] L. H. Xiong, H. B. Lou, X. D. Wang, T. T. Debela, Q. P. Cao, D. X. Zhang, S. Y. Wang, C. Z. Wang, and J. Z. Jiang, Evolution of local atomic structure during solidification of Al_2Au liquid: An *ab initio* study, Acta Mater. **68**, 1 (2014).

[4] M. Rieth, S. L. Dudarev, S. M. G. de Vicente, J. Aktaa, T. Ahlgren, S. Autusch, D. E. J. Armstrong, M. Balden, N. Baluc, M. F. Barthe *et al.*, Recent progress in research on tungsten materials for nuclear fusion applications in Europe, J. Nucl. Mater. **432**, 482 (2013).

[5] L. Xing, X. Liu, Z. Cao, C. He, and J. Liu, Effect of increasing Ti content on the phase, interface, dynamic mechanical properties and ballistic performance of W–Ti–Zr alloys, Mater. Sci. Eng. A **831**, 142196 (2022).

[6] O. N. Senkov, S. Gorsse, and D. B. Miracle, High temperature strength of refractory complex concentrated alloys, Acta Mater. **175**, 394 (2019).

[7] K. Fritz, S. Wimmer, H. Ebert, and M. Meinert, Large spin Hall effect in an amorphous binary alloy, Phys. Rev. B **98**, 094433 (2018).

[8] V. V. Ozherelyev, A. I. Bocharov, A. V. Bondarev, and Y. V. Barmin, X-ray diffraction study of atomic structure of Hf-W amorphous alloys, Int. J. Refract. Met. Hard Mater. **48**, 141 (2015).

[9] A. M. Mullis, O. E. Jegede, T. D. Bigg, and R. F. Cochrane, Dynamics of core-shell particle formation in drop-tube processed metastable monotectic alloys, Acta Mater. **188**, 591 (2020).

[10] A. Jakhar, A. Bhattacharya, P. Rath, and S. K. Mahapatra, Effect of thermal anisotropy on binary alloy dendrite growth, Int. J. Heat Mass Transfer **127**, 1114 (2018).

[11] B. Hutchinson, J. Komenda, S. Kada, M. Barnett, and A. Oskarsson, Observations on remarkable texture in cast zinc, Scr. Mater. **166**, 78 (2019).

[12] P. Ganesh and M. Widom, Liquid-liquid transition in supercooled silicon determined by first-principles simulation, Phys. Rev. Lett. **102**, 075701 (2009).

[13] T. Ishikawa and P. F. Paradis, Thermophysical properties of molten refractory metals measured by an electrostatic levitator, J. Electron. Mater. **34**, 1526 (2005).

[14] T. Ishikawa, P. F. Paradis, T. Itami, and S. Yoda, Thermophysical properties of liquid refractory metals: Comparison between hard sphere model calculation and electrostatic levitation measurements, J. Chem. Phys. **118**, 7912 (2003).

[15] V. L. Deringer and G. Csanyi, Machine learning based interatomic potential for amorphous carbon, Phys. Rev. B **95**, 094203 (2017).

[16] Z. Y. Fan, Z. Z. Zeng, C. Z. Zhang, Y. Z. Wang, K. K. Song, H. K. Dong, Y. Chen, and T. A. Nissila, Neuroevolution machine learning potentials: Combining high accuracy and low cost in atomistic simulations and application to heat transport, Phys. Rev. B **104**, 104309 (2021).

[17] A. P. Bartók, R. Kondor, and G. Csányi, On representing chemical environments, Phys. Rev. B **87**, 184115 (2013).

[18] R. M. Balabin and E. I. Lomakina, Support vector machine regression (LS-SVM)—An alternative to artificial neural networks (ANNs) for the analysis of quantum chemistry data?, Phys. Chem. Chem. Phys. **13**, 11710 (2011).

[19] H. Tang, Y. Zhang, Q. J. Li, H. W. Xu, Y. C. Wang, Y. Z. Wang, and J. Li, High accuracy neural network interatomic potential for NiTi shape memory alloy, Acta Mater. **238**, 118217 (2022).

[20] X. Y. Wang, Y. A. Wang, L. F. Zhang, F. Z. Dai, and H. Wang, A tungsten deep neural-network potential for simulating mechanical property degradation under fusion service environment, Nucl. Fusion **62**, 126013 (2022).

[21] R. E. Ryltsev and N. M. Chtchelkatchev, Deep machine learning potentials for multicomponent metallic melts: Development, predictability and compositional transferability, J. Mol. Liq. **349**, 118181 (2022).

[22] R. L. Xiao, Q. Wang, J. Y. Qin, J. F. Zhao, Y. Ruan, H. P. Wang, H. Li, and B. Wei, A deep learning approach to predict thermophysical properties of metastable liquid Ti-Ni-Cr-Al alloy, J. Appl. Phys. **133**, 085102 (2023).

[23] R. L. Xiao, K. L. Liu, Y. Ruan, and B. Wei, Rapid acquisition of liquid thermophysical properties from pure metals to quaternary alloys by proposing a machine learning strategy, Appl. Phys. Lett. **123**, 052204 (2023).

[24] L. F. Zhang, D. Y. Lin, H. Wang, R. Car, and Weinan E., Active learning of uniformly accurate interatomic potentials for materials simulation, Phys. Rev. Mater. **3**, 023804 (2019).

[25] Y. Z. Zhang, H. D. Wang, W. J. Chen, J. Z. Zeng, L. F. Zhang, H. Wang, and Weinan E., DP-GEN: A concurrent learning platform for the generation of reliable deep learning based potential energy models, Comput. Phys. Commun. **253**, 107206 (2020).

[26] L. H. Li, L. Hu, S. J. Yang, W. L. Wang, and B. Wei, Thermodynamic properties and solidification kinetics of intermetallic Ni_7Zr_2 alloy investigated by electrostatic levitation technique and theoretical calculations, J. Appl. Phys. **119**, 035902 (2016).

[27] P. F. Paradis, T. Ishikawa, and S. Yoda, Noncontact density measurements of tantalum and rhenium in the liquid and undercooled states, Appl. Phys. Lett. **83**, 4047 (2003).

[28] A. P. Thompson, H. M. Aktulga, R. Berger, D. S. Bolintineanu, W. M. Brown, P. S. Crozier, P. J. in't Veld, A. Kohlmeyer, S. G. Moore, T. D. Nguyen *et al.*, LAMMPS—A flexible simulation tool for particle-based materials modeling at the atomic, meso, and continuum scales, Comput. Phys. Commun. **271**, 108171 (2022).

[29] H. Wang, L. F. Zhang, J. Q. Han, and Weinan E., DeePMD-kit: A deep learning package for many-body potential energy representation and molecular dynamics, Comput. Phys. Commun. **228**, 178 (2018).

[30] L. Zhang, J. Han, H. Wang, W. A. Saidi, R. Car, and Weinan E., in *Advances in Neural Information Processing Systems*, edited by S. Bengio, H. Wallach, H. Larochelle, K. Grauman, N. Cesa-Bianchi, and R. Garnett (Curran Associates, 2018), pp. 4441–4451.

[31] M. J. P. Nijmeijer, A. F. Bakker, C. Bruin, and J. H. Sikkenk, A molecular-dynamics simulation of the lennard-jones liquid vapor interface, J. Chem. Phys. **89**, 3789 (1988).

[32] R. L. Xiao, Y. Ruan, M. J. Lin, J. Y. Qin, H. Li, L. Hu, and B. B. Wei, Metastable liquid properties and rapid crystal growth of Ti-Ni-Al alloy investigated by electrostatic levitation and molecular dynamics simulation, Sci. China Technol. Sci. **64**, 2200 (2021).

[33] J. Brillo and I. Egry, Density and excess volume of liquid copper, nickel, iron, and their binary alloys, Int. J. Mater. Res. **95**, 691 (2004).

[34] I. Egry, E. Ricci, R. Novakovic, and S. Ozawa, Surface tension of liquid metals and alloys—Recent developments, Adv. Colloid Interface Sci. **159**, 198 (2010).

[35] Y. Nagata, T. Ohto, M. Bonn, and T. D. Kuhne, Surface tension of *ab initio* liquid water at the water-air interface, J. Chem. Phys. **144**, 204705 (2016).

[36] Y. R. Guo, C. Qiao, J. J. Wang, H. Shen, S. Y. Wang, Y. X. Zheng, R. J. Zhang, L. Y. Chen, W. S. Su, C. Z. Wang *et al.*, Bergman-type medium range order in amorphous $Zr_{77}Rh_{23}$ alloy studied by ab initio molecular dynamics simulations, J. Alloys Compd. **790**, 675 (2019).

[37] J. Kang, J. Zhu, S. H. Wei, E. Schwegler, and Y. H. Kim, Persistent medium-range order and anomalous liquid properties of $Al_{1-x}Cu_x$ alloys, Phys. Rev. Lett. **108**, 115901 (2012).

[38] J. Akola and R. O. Jones, Structural phase transitions on the nanoscale: The crucial pattern in the phase-change materials $Ge_2Sb_2Te_5$ and GeTe, Phys. Rev. B **76**, 235201 (2007).

[39] Y. C. Liang, R. S. Liu, Y. F. Mo, H. R. Liu, Z. A. Tian, Q. Y. Zhou, H. T. Zhang, L. L. Zhou, Z. Y. Hou, and P. Peng, Influence of icosahedral order on the second peak splitting of pair distribution function for $Mg_{70}Zn_{30}$ metallic glass, J. Alloys Compd. **597**, 269 (2014).

[40] S. P. Pan, J. Y. Qin, W. M. Wang, and T. K. Gu, Origin of splitting of the second peak in the pair-distribution function for metallic glasses, Phys. Rev. B **84**, 092201 (2011).

[41] I. M. Kirian, A. D. Rud, O. S. Roik, V. P. Kazimirov, O. M. Yakovenko, and A. M. Lakhnik, Local atomic structure of liquid $Al_{87}Mg_{13}$ alloy, J. NonCryst. Solids **586**, 121562 (2022).

[42] J. M. Cowley, Short-range order and long-range order parameters, Phys. Rev. **138**, A1384 (1965).

[43] M. Celtek, U. Domekeli, S. Sengul, and C. Canan, Effects of Ag or Al addition to CuZr-based metallic alloys on glass formation and structural evolution: A molecular dynamics simulation study, Intermetallics **128**, 107023 (2021).

[44] P. Ganesh and M. Widom, Signature of nearly icosahedral structures in liquid and supercooled liquid copper, Phys. Rev. B **74**, 134205 (2006).

[45] F. Duan and J. Guojun, *Introduction to Condensed Matter Physics* (World Scientific, Singapore, 2005).

[46] J. D. Honeycutt and H. C. Andersen, Molecular-dynamics study of melting and freezing of small Lennard-Jones clusters, J. Phys. Chem. **91**, 4950 (1987).

[47] M. Shimono and H. Onodera, Structural relaxation in supercooled liquids, Mater. Trans. **46**, 2830 (2005).

[48] P. Ganesh and M. Widom, *Ab initio* simulations of geometrical frustration in supercooled liquid Fe and Fe-based metallic glass, Phys. Rev. B **77**, 014205 (2008).

[49] X. L. Wang, Y. Dong, M. Mohr, H. J. Fecht, X. D. Wang, Q. P. Cao, D. X. Zhang, Z. W. Dai, and J. Z. Jiang, Correlation between viscosity and local atomic structure in liquid $Zr_{56}Co_{28}Al_{16}$ alloy, Microgr. Sci. Technol. **34**, 10 (2022).